metals

MDPI

Article

Precipitation Kinetics and Evaluation of the Interfacial Mobility of Precipitates in an AlSi7Cu3.5Mg0.15 Cast Alloy with Zr and V Additions

Pierre Heugue [1], Daniel Larouche [1,*], Francis Breton [2], Denis Massinon [3], Rémi Martinez [4] and X.-Grant Chen [5]

1 Department of Mining, Metallurgy and Materials Engineering, Aluminum Research Center—REGAL, Laval University, 1065, ave de la Médecine, Québec, QC G1V 0A6, Canada
2 Rio Tinto, Arvida Research and Development Centre, 1955, Mellon Blvd, Saguenay, Québec, QC G7S 4K8, Canada
3 Linamar Montupet Light Metal Division, 3, rue de Nogent, 60290 Laigneville, France
4 Linamar Corporation—The Center, 700 Woodlawn Road West, Guelph, ON N1K 1G4, Canada
5 Department of Applied Sciences, University of Québec at Chicoutimi, 555, boul. de l'Université, Saguenay, QC G7H 2B1, Canada
* Correspondence: Daniel.Larouche@gmn.ulaval.ca; Tel.: +1-418-656-2153

Received: 10 June 2019; Accepted: 9 July 2019; Published: 11 July 2019

Abstract: Recent environmental restrictions constrained car manufacturers to promote cast aluminum alloys working at high temperatures (180 °C–300 °C). The development of new alloys permits the fabrication of higher-strength components in engine downsizing. Those technologies increase internal loadings and specific power and stretch current materials to their limits. Transition metals in aluminum alloys are good candidates to improve physical, mechanical, and thermodynamic properties with the aim of increasing service life of parts. This study is focused on the modified AlSi7Cu3.5Mg0.15 alloy where Mn, Zr, and V have been added as alloying elements for high-temperature applications. The characterization of the cast alloy in this study helps to evaluate and understand its performance according to their physical state: As-cast, as-quenched, or artificially aged. The precipitation kinetics of the AlSi7Cu3.5Mg0.15 (Mn, Zr, V) alloy has been characterized by differential scanning calorimetry (DSC), transmission electron microscopy (TEM) observations, and micro-hardness testing. The Kissinger analysis was applied to extract activation energies from non-isothermal DSC runs conducted at different stationary heating rates. Finally, first-order evaluations of the interfacial mobility of precipitates were obtained.

Keywords: AlSi7Cu3.5Mg0.15 alloy; interfacial mobility; differential scanning calorimetry (DSC); precipitation kinetics; Kissinger methodology

1. Introduction

Due to poor mechanical properties and high malleability of pure aluminum, alloying elements are added before casting to improve physical and mechanical properties [1]; such as Si for casting properties (castability, cold crack capability, wear resistance, shrinkage behavior), Mg, and Cu to generate precipitation hardening systems. In the automotive industry, aluminum hypoeutectic alloys (<12% Si) with Cu and Mg additions are mostly subject to precipitation hardening heat treatment [2]. The best mechanical properties are associated with the formation of precipitates through an optimum heat treatment sequence, generally including: Solutionizing, water quenching, and artificial aging [3].

During this sequence, the resulting decomposition of the supersaturated solid solution produces a size distribution of precipitates, which directly affects the final mechanical properties.

Heat treatment (HT) corresponds to the last metallurgical step of the overall manufacturing process. Optimizing the heat-treating process is essential to improve the overall performances of the castings. Therefore, understanding and characterizing the effect of the quenching rate and other HT parameters are necessary to limit for instance the impact of residual stresses while maintaining the hardening potential.

Precipitation in aluminum–copper alloy (Cu wt% ranging from 1 to 4.5) has mostly been studied by researchers as an elementary case. The full concomitant precipitation sequence of binary Al–Cu alloy during aging is presented below [4].

Supersaturated solid solution → atomic clusters → GPI zones → GPII (θ′′) → θ′ → θ

The morphology of the metastable precipitates is disk-like. In ternary Al–Mg–Si alloys, the following precipitation sequence is observed [5].

Supersaturated solid solution → atomic clusters → GPI zones → β′′ → β′ → β

The metastable precipitates have a needle-like morphology in this sequence. At high aging temperatures, Si-free phases can appear as irregular plates in the matrix.

Quaternary Al–Si–Cu–Mg alloys show an impressive complexity in their own precipitation sequence due to the combination of the concomitant sequences and the formation of the Q (Al–Si–Cu–Mg) phase and its precursors. Different studies have shown the effect of composition ratios in such alloys to explain the nature of hardening precipitates and the conditions under which they are formed [6–10]. Furthermore, Q phase precursors present a vast topic in literature due to their sophisticated structure [11]. Unfortunately, precipitation kinetics data are missing, and the majority of studies focus on phase identification according to isothermal aging conditions.

Aluminum alloys used for the manufacture of automotive cylinder heads are mainly derived from the hypo-eutectic Al–Si family. Recent alloy compositions have been developed in order to upgrade their strength at higher temperatures via the formation of thermally stable and coarsened resistant phases. Among the transition metals, V and Zr have low diffusivity and solubility in Al matrix and do not impact castability, ductility, and fracture toughness. They form thermally stable complex intermetallics helping to maintain the strength at temperatures up to 350 °C, with the precipitation of Al_3Zr, $Al_{21}V_2$, or Al_3(Zr, V, Ti) dispersoids [12–15], with occasional small amounts of Si by substitution of Al [16].

Some theoretical models have been proposed to calculate the evolution of precipitates during aging. These mathematical models were developed with major simplifications, like assuming that precipitates are spherical, nucleation is homogenous, and that local equilibrium prevails at the interface [17–20]. More recently, in order to improve and explain the paradox regarding the interface velocity during the initial stage of nucleation-growth processes, Larouche [21] developed another theoretical approach, which is based on the mixed-mode analytical solution of the mass conservation equation, which assumes that growth is not only controlled by the concentration gradients in front of the precipitate, but also by the mobility of the interface. This theory proposes that the subcritical growth regime occurring during nucleation can be described as a one-stage process for which the activation energy is associated to the mobility of the interface. The characterization of this parameter was first attempted and described in [22] for θ′-Al_2Cu and θ-Al_2Cu precipitates in a binary Al-3.5 wt%Cu. The evaluation of the interface mobility was made from the analysis of isochronal differential scanning calorimetric (DSC) runs, including the evaluation of thermodynamic variables and the number density of precipitates. The developed methodology remains to be applied for all kinds of age-hardenable alloys. The present study is a direct application of this method for the AlSi7Cu3.5Mg0.15 (Mn, Zr, V), which will be compared to the binary Al-3.5 wt%Cu.

The first part of the paper will be dedicated to understanding the impact of the solution heat treatment (SHT) on secondary phases, including the dispersoids containing Zr or V. The second part will describe the calorimetric analysis performed with different heating rates on supersaturated samples.

This analysis will be conducted in order to estimate the interfacial mobility of the main hardening precipitates. Finally, the precipitation kinetics of the alloy will be compared with the precipitation kinetics of a binary Al-3.5 wt%Cu alloy, highlighting the role of silicon in the system.

2. Experimental

2.1. Samples Preparation

The AlSi7Cu3.5Mg0.1 (Mn, Zr, V) alloy ingots were first elaborated by RioTinto (Saguenay, QC, Canada). Cylindrical samples (ø 21 mm, 200 mm length) have been cast in the R&D center of Montupet (Laigneville, France) by the gravity die-casting technique using a thermo-regulated metallic mold according to the NF A57-702-1981 AFNOR standard with Sr modification beforehand. The chemical composition of the studied cast aluminum alloy was analyzed by inductively coupled plasma-atomic emission spectroscopy (ICP-AES) using the IRIS intrepid analyzer of Thermo Fischer Scientific (Waltham, MA, USA). The composition is given in Table 1. Quality monitoring during the casting was performed with solidified alloy density measurements, repetitive degassing of the melting bath (every 10 castings), and chemical composition controls. Casting conditions were optimized (mold and metal temperatures) in order to obtain a secondary dendrite arm spacing (SDAS) between 15 and 25 µm, representative of those observed in a cylinder fire deck surface [23]. Samples were thus cast under the following conditions: 709 °C ± 6 °C in the ladle at the time of casting and in the die at 149 °C ± 6 °C. The solution heat treatment of the AlSi7Cu3.5Mg0.1 (Mn, Zr, V) alloy was performed at 505 °C during 4 h with an initial slow heating rate of 6.5 K/min and followed by a cold-water quench to obtain the maximum solute supersaturation.

Table 1. General chemical composition of cast alloy from cast ingots.

AlSi7Cu3.5Mg0.15 (Mn, Zr, V)	Elements	Si	Cu	Mg	Fe	Ti	Mn	Zr	V	Sr	Zn
	wt%	6.86	3.41	0.14	0.12	0.11	0.15	0.12	0.11	0.013	0.014

2.2. Characterization Methods

2.2.1. AlSi7Cu3.5Mg0.15 (Mn, Zr, V) As-Cast and As-Quenched Characterization

The AlSi7Cu3.5Mg0.1 (Mn, Zr, V) alloy samples have been characterized initially through their metallurgical condition. Samples for microstructural examination were sectioned from the cast cylinders, mounted, ground, and polished using the standard procedure. The polished sections were then examined with an optical microscope and with electron probe microanalysis (EPMA-CAMECA SX100 with W filament, Cameca SAS, Paris, France) equipped with a wavelength dispersive spectrometer (WDS). Scanning electron microscopy (SEM) observations have been conducted on a FEI QUANTA-250 (Thermo Scientific Quanta, Hillsboro, OR, USA) assisted by an energy dispersive spectrometer(EDS). The samples were coated by 10–20 nm thick layers of gold and palladium prior to examination to improve their electrical conductivity. Intermetallic phases were identified by comparison with their description in the literature [24,25] and also from as-cast microprobe mapping analysis especially for Al_2Si_2Sr (brown on micrographs), α-Al(Fe, Cu, Mn)Si (major occurrence; polyhedral, Chinese script morphology) and Al_2Cu (high Cu atomic mass; rounded morphology) phases.

2.2.2. Power Compensation Differential Scanning Calorimetry of Quenched Specimens

Samples of 4.5 mm diameter, and 2 mm thickness were taken from quenched cylinders for DSC analysis with the PerkinElmer Diamond instrument. The latter was calibrated for one heating rate (12.5 °C/min). The specimens were held for few hours at room temperature before their heating in the DSC device in order to limit the effects of natural aging. The reference furnace contained a pure aluminum sample for each scan. Measurements were conducted with all samples and references prepared with the exact same mass (±0.01 mg). The instrumental baselines were performed with pure

aluminum in the sample and reference furnaces for each heating rates. The methodology of baseline graphical modifications to correct the results was a two-step process, where the instrumental baseline was first subtracted from the measured DSC result, and then a calculated baseline with a polynomial function was subtracted from the latter. Constant heating rates of 1, 2, 4, 6, and 8 K/min were applied, and two different samples were analyzed for each heating rate for reproducibility.

2.2.3. Microhardness, TEM Preparation, and Observations

Samples for microhardness examination were sectioned from the quenched cylinder, mounted, ground, and polished using the standard procedure. The polished sections were then evaluated with an optical microscope. Isothermal aging at 190 °C was interrupted at different times by quenching the sample in order to subject them to Vickers microhardness tests at room temperature. The aging temperature was chosen for comparison purposes with [22] and [26]. Microhardness experiments were conducted on Clemex CMT (Longueuil, QC, Canada) using a load of 0.0098 N with a dwell time of 13 s. To ascertain reproducibility and statistical validity, 10–16 microhardness tests were performed at each condition. Only intradentritic measurements were performed. Vickers microhardness indentation showing difference in the lengths of the diagonals over 5% of the mean was discarded. The typical accuracy obtained from the standard deviation in a set of hardness data according to the number of indentations was about ±3 HV.

TEM samples were cut from quenched cylinders and were aged at four conditions (at 190 °C for 30 min and 6 h, at 350 °C for 1 h and 12 h) and have been prepared by electro-polishing. Precipitates observations by transmission electron microscopy on Al matrix plans for the different aging conditions have been performed with the Jeol JEM-2100F TEM (JEOL Inc., Tokyo, Japan) on 2F-1g or 2g matrix condition in g200 of aluminum near [001] axis and also in g200 near [011] axis. Three kinds of analysis have been elaborated. First, EDS and selected area electron diffraction (SAED) analysis were used for phase identification. Second, electron energy loss spectroscopy (EELS) using the log-ratio technique was applied for sample thickness evaluation in order to calculate the number density of precipitates.

3. Results

3.1. Metallurgical Characterization

The as-cast AlSi7Cu3.5Mg0.15 (Mn, Zr, V) samples present millimetric grain size and a measured SDAS of 17.6 µm ± 3.2 µm. Microstructures show very low porosity. The intermetallic phases were identified based on literature [25], thermodynamic computations, and the as-cast microprobe mapping analysis. Intermetallic phases like: α-Al(Fe, Cu, Mn)Si, β-AlFeSi, Al_2Cu, Al_7Cu_2Fe, Al_3 (Zr, Ti, V), Al_2Si_2 (Sr) have been identified. Phase formation was simulated with the Scheil module of Thermo-Calc [27] and the TTAL7 [28] database to estimate the mass fractions of solid phases formed during solidification. The evolution of volume fraction of the potential phases has been calculated and was in qualitative agreement with those observed in the micrographs. Quantitative measurements of the chemical composition through an as-cast dendrite have been performed on the microprobe by linear scanning analysis. The distribution of Mn, Zr, V, and Mg show slight variations in the 0.05–0.15 wt% range, while Si and Cu compositions show larger concentration gradients inside the dendrites. Indeed, Cu content drops across the dendrite from 2.0 wt% at the boundary to 0.5 wt% near the center. Si content is very high (>5 wt%) at the periphery of the dendrites, drops drastically to 0.75 wt% in a depleted 2 to 7 µm thick zone, to finally remain uniform at 1.5 wt% in the core of the dendrite.

Figure 1 presents the microstructure resulting from the SHT and quench. One can see that the silicon platelets were spheroidized and that many of the intermetallics were dissolved. The residual undissolved intermetallics are identified in Figure 1. The microprobe mapping analysis presented in Figure 2 validates the identification. The equilibrium calculation performed with Thermo-Calc at 505 °C showed that the undissolved intermetallics were α Al(Fe, Cu, Mn)Si, Al_2Si_2 (Sr), and Al_3(Zr, V, Ti)

dispersoids. Obviously, the main undissolved secondary phase was silicon. The chemical composition in the dendrites was found to be uniform after the SHT, as this was confirmed by a linear-scanning EPMA, especially for Si and Cu. The amounts of Si and Cu dissolved in the dendrites were respectively estimated to be 1.0 wt% and 2.8 wt%.

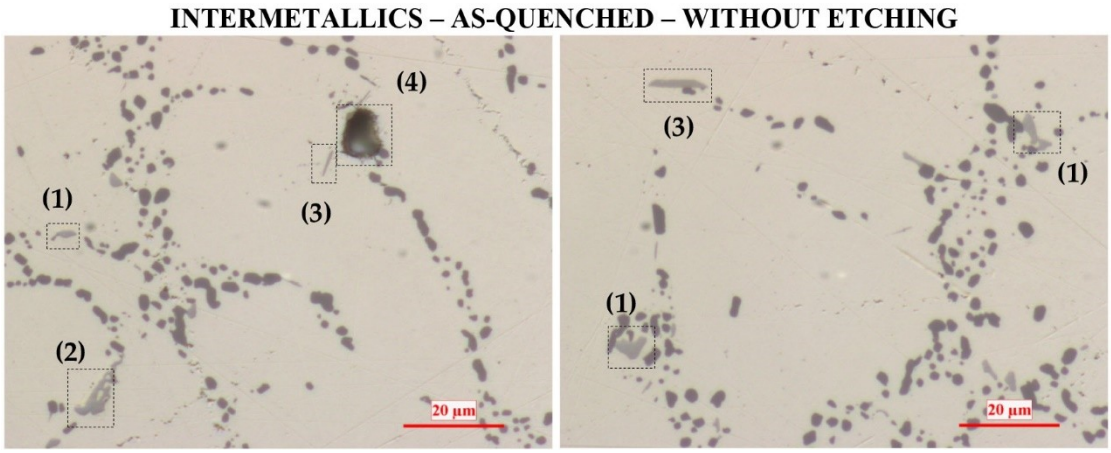

Figure 1. As-quenched intermetallics found in the AlSi7Cu3.5Mg0.15 (Mn, Zr, V) alloy microstructure. (1) Al_7Cu_2Fe or Al_3(Zr,V), (2) α Al(FeMn)Si, (3) β-AlFeSi, (4) H_2 pore.

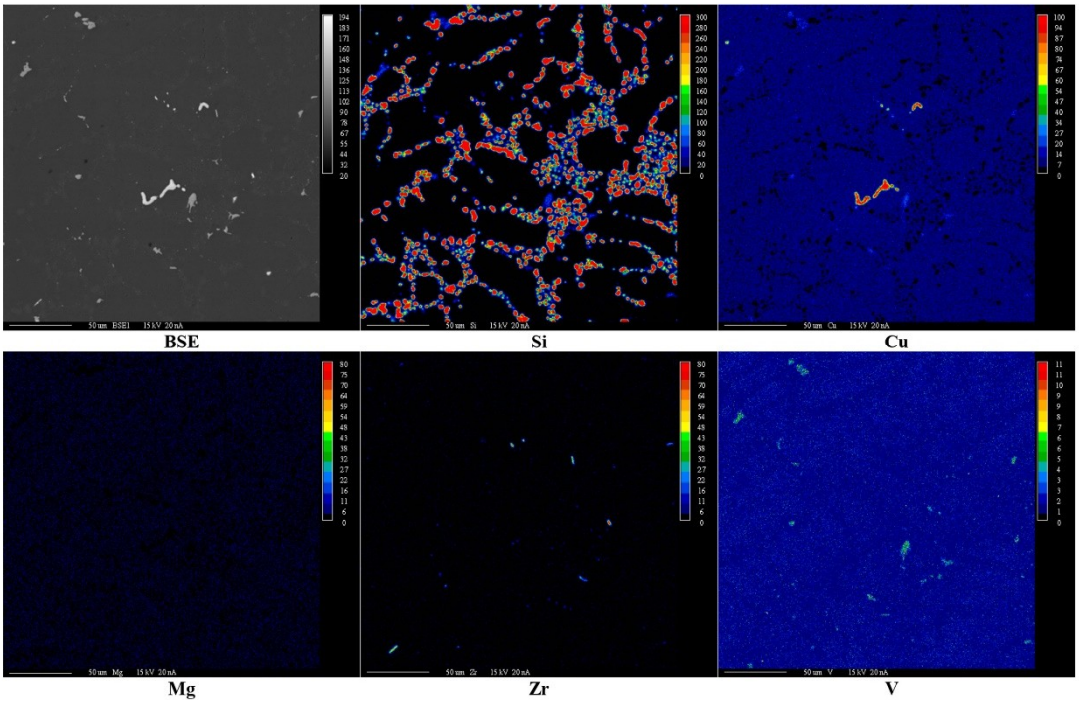

Figure 2. As-quenched microprobe cartography (1 pixel for 0.5 µm).

3.2. DSC Runs for Different Constant Heating Rates

The isochronal methodology described in [22] was followed and Figure 3 shows the precipitation peaks obtained with five different heating rates. Three exothermic precipitation peaks labelled A, B, and C are particularly interesting and were considered for further analysis.

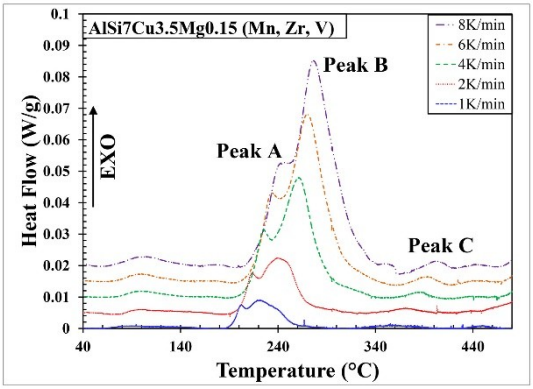

Figure 3. Differential scanning calorimetry (DSC) runs made with 1, 2, 4, 6, and 8 K/min heating rates for as-quenched AlSi7Cu3.5Mg0.15 (Mn, Zr, V) alloy.

3.3. Determination of Kinetic Parameters by the Kissinger Method

The Kissinger methodology was applied to analyze the precipitation kinetics of the alloy. Table 2 summarizes the measured peak temperatures obtained at different heating rates for the two sets of data and Figure 4 presents the Kissinger diagrams obtained. The generic kinetic equation proposed by Lee and Kim [29] and Starink and Zhara [30] (LKSZ) was used for the determination of the kinetic parameters. According to the LKSZ equation, the fraction of phase transformation α evolves with time as follows:

$$\alpha = 1 - \left(1 + c \cdot (k \cdot t)^n\right)^{-\frac{1}{c}} \quad (1)$$

where t is the time and c, k, and n are the three independent kinetic parameters. The parameter n is set equal to 3, since we consider that the nucleation sites are saturated after the quench. Consequently, the rest of the transformation can be modelled as a single-stage reaction for which k follows an Arrhenius-type dependence with temperature, which is expressed as follows:

$$k = k_0 \exp\left(-\frac{E}{RT}\right). \quad (2)$$

Table 2. DSC peak temperatures $T_f = T_{Peak}$ obtained at different heating rates for the AlSi7Cu3.5Mg0.15 (Mn, Zr, V) alloy.

Heating Rate (K/min)	Peak A		Peak B		Peak C	
1	206.3	204.6	223.2	221.3	353.3	355.3
2	217.9	214.6	243.2	239.3	372.1	373.3
4	225.9	226.0	262.5	261.3	384.8	385.6
6	234.5	234.5	270.8	269.8	391.6	393.3
8	247.5	244.5	276.2	276.7	401.1	403.5

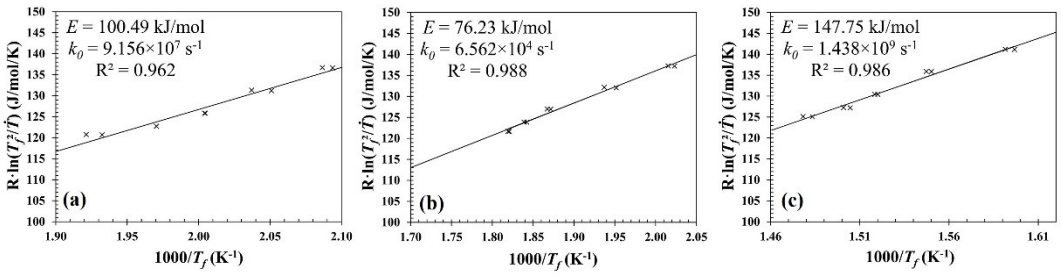

Figure 4. Kissinger diagrams for AlSi7Cu3.5Mg0.15 (Mn, Zr, V) alloy: (**a**) Peak A, (**b**) peak B, (**c**) peak C.

The impingement factor (c) can be estimated by fitting the LKSZ equation on the experimental DSC curve $d\alpha/dt$, the latter being determined from the following equation [31]:

$$\frac{d\alpha}{dt} = \frac{1}{\Delta h}(q - q_B) \tag{3}$$

where q is the power measured by the DSC, q_B is the baseline and Δh is the total latent heat released during the reaction. Figure 5 presents the fitting obtained for a 6 K/min heating rate analysis. Fitting is not perfect due to the dissolution process of each coherent/semi-coherent phases, which have not been taken into account in the analysis. Activation energies E and the values for k_0 are presented in Table 3. Precipitation peaks have been identified according to literature, TEM observations and by comparison to metastable phase diagram using MatCalc v. 5.62 [32]. Major peaks A, B, and C correspond to the growth of the Guinier–Preston (GP) zones + β'' + Q', θ'-Al_2Cu and θ-Al_2Cu, respectively. The formation of GP zones is assumed here to be a continuous process, where Cu monolayers pile up producing the so-called θ'' precipitates [33].

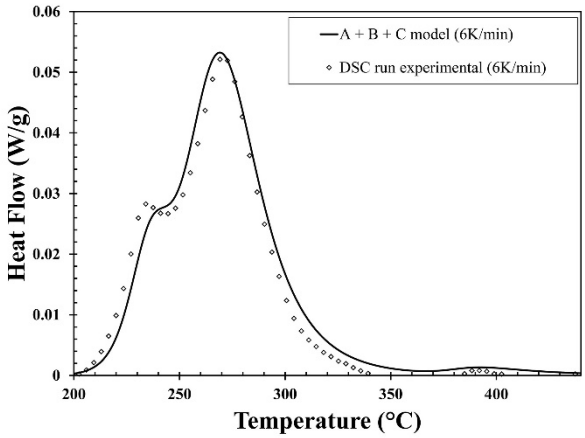

Figure 5. DSC run and peaks (A, B, C) adjusted to optimize the fit between experimental and sum of the heat produced by associated transformations for AlSi7Cu3.5Mg0.15 (Mn, Zr, V) alloy.

Table 3. Parameters from the fitting procedure for AlSi7Cu3.5Mg0.15 (Mn, Zr, V) alloy.

Peak	Precipitate	E (kJ/mol)	k_0 (s^{-1})	n	c	Δh (mJ)
A	GP zones + β'' + Q'	100.49	9.156×10^7	3	1	5.59
B	θ'	76.23	6.562×10^4	3	1.7	27.3
C	θ	147.75	1.438×10^9	3	4	0.745

3.4. Comparison of Isothermal Evolution from LKSZ Kinetic Model with Microhardness

Figure 6 presents the isothermal evolution of fractions transformed for each peak at 190 °C and 350 °C as predicted by the LKSZ kinetic model. According to this model and the kinetic parameters determined above, it takes less than 1 h to obtain a small but definite fraction transformed at 190 °C for peaks A and B in the studied AlSi7Cu3.5Mg0.15 (Mn, Zr, V) alloy. At 350 °C, reactions associated with peaks A and B progress almost instantaneously while the reaction associated to peak C progresses steadily since the beginning of aging. Similar results about kinetics of precipitation in Al–Si–Cu alloys were reported by [13,34–36]. Microhardness evolution measurements during aging at 190 °C show changes in phase formation occurring between 0.5 and 2 h for the AlSi7Cu3.5Mg0.15 (Mn, Zr, V) alloy, as revealed by the significant increase in hardness value. Similar microhardness results were obtained in the work of Tabibian et al. [37] and Ovono Ovono et al. [36].

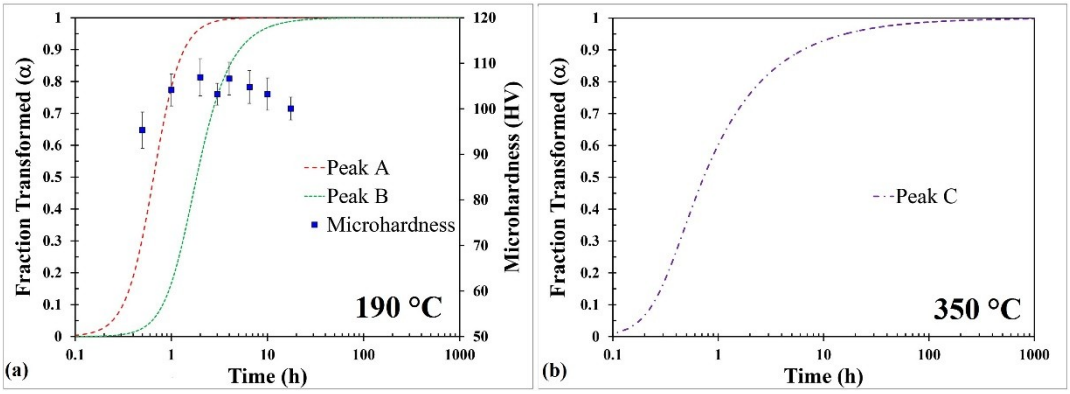

Figure 6. Isothermal evolution of the fraction transformed α in the AlSi7Cu3.5Mg0.15 (Mn, Zr, V) alloy as calculated with the LKSZ kinetic equation (**a**) for peaks A and B at 190 °C associated with microhardness results during aging, and (**b**) for peak C at 350 °C.

3.5. TEM Precipitate Observations

Transmission electron microscopic examinations were conducted on samples artificially aged at 190 °C during 30 min and 6 h and at 350 °C during 1 h and 12 h. The observations made near the [001] and [011] axis zone of g200 beam condition are presented in Figure 7. For aging at 190 °C, disk-shaped semi-coherent θ′-Al_2Cu metastable phases were observed and identified using the dark field diffraction patterns. θ′-Al_2Cu precipitate size evolution and number density are presented in Table 4. For the AlSi7Cu3.5Mg0.15 (Mn, Zr, V) alloy, two other kinds of precipitates can be observed: Dark rounded ones, identified as Al_3(Zr, V, Ti) dispersoids, and small dark dots of β′′ or Q′ (globular, needles). They were identified with the help of EDS analysis and literature data [6–8]. These identifications are detailed in Figure 8a. Overall precipitate number density for combined Q′ and β′′ is $6.5 \pm 1.8 \times 10^{21}$ sites/m^3. A clear distinction between these phases was not possible because of the insufficient resolution of the TEM. In some regions, some small incoherent stable precipitates (≤250 nm in length) are present. These particles were identified as θ-Al_2Cu phase by SAED analysis. Three major kinds of precipitates can be identified in samples aged at 350 °C. All precipitates are incoherent with Al matrix and are associated, as detailed in Figure 8b, with the θ-Al_2Cu stable phase (small grey dispersoids), the Si precipitates (big globular dark ones), and the Al_3 (Zr, V, Ti) precipitates (small dark rounded). The latter have not evolved in size nor in number density relative to the previous aging condition. A combined number density of 1.0×10^{20} sites/m^3 was averaged for the θ-Al_2Cu precipitates found in samples aged at 350 °C during 1 and 12 h.

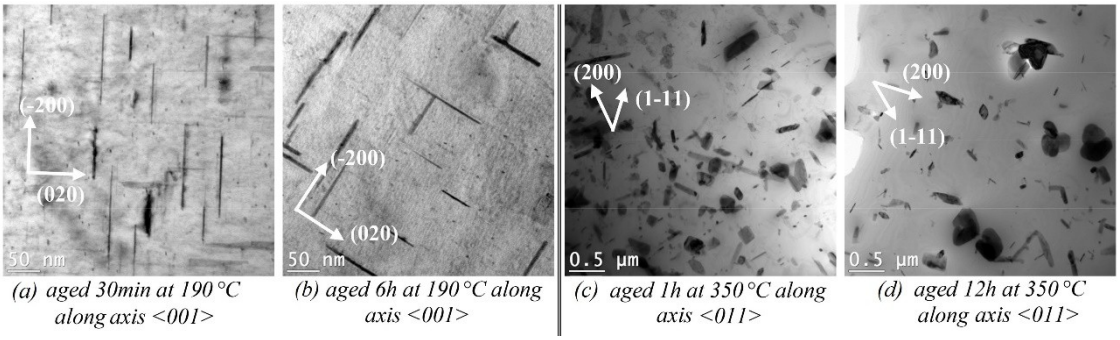

(a) aged 30min at 190 °C along axis <001> *(b) aged 6h at 190 °C along axis <001>* *(c) aged 1h at 350 °C along axis <011>* *(d) aged 12h at 350 °C along axis <011>*

Figure 7. TEM observations for the AlSi7Cu3.5Mg0.15 (Mn, Zr, V) alloy in g200 beam condition.

Table 4. θ′-Al_2Cu precipitate size and number density evolutions for different aging conditions at 190 °C for the AlSi7Cu3.5Mg0.15 (Mn, Zr, V) alloy.

Length (nm)		Precipitate Density (sites/m^3)	
30 min	6 h	30 min	6 h
88 ± 30	105 ± 36	$8.6 \pm 1.2 \times 10^{20}$	$6.8 \pm 1.3 \times 10^{20}$

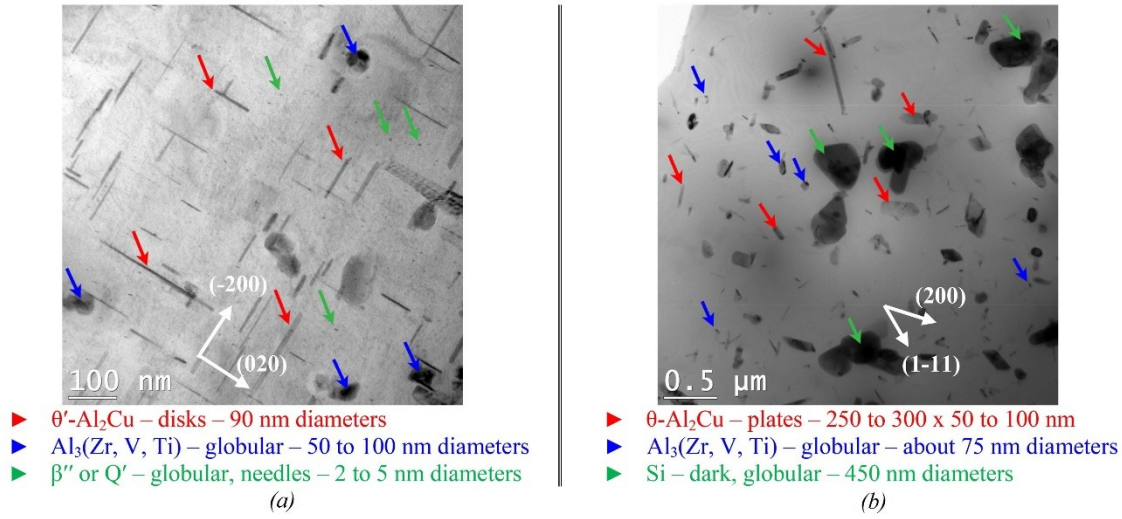

Figure 8. Detailed precipitate identification in the AlSi7Cu3.5Mg0.15 (Mn, Zr, V) alloy for aging (**a**) at 190 °C during 6 h; (**b**) at 350 °C during 12 h.

3.6. Evaluation of Interfacial Mobilities in AlSi7Cu3.5Mg0.15 (Mn, Zr, V) Alloy

The evaluation of interfacial mobilities was made using Equations (24) and (25) of [22], with the kinetic parameters listed above. The relevant equations are rewritten below:

$$M = \frac{\Omega}{RT} \exp\left(-\frac{E}{RT}\right), \tag{4}$$

$$\Omega = \frac{V_m \cdot k_0}{\left(\frac{N_0 \cdot A_1}{g_\phi^{eq}}\right)^{1/3} \sum_{i=1}^{I} c_\phi^i \cdot \ln\left(\frac{\bar{c}_i}{c_{i\,eq}^*}\right)}. \tag{5}$$

The parameter *A1*, which is related to the shape of the particles, was roughly estimated by assuming that θ-Al_2Cu precipitates and precursors (θ″ and θ′) were growing as oblate spheroids with a typical aspect ratio of 20. This makes A_1 = 0.209. For the needle-shaped β″ precipitates (prolate spheroids), a shape factor of 9 was estimated giving A_1 = 0.052. For Q′ spherical precipitates, $A_1 = 4\pi/3$. The molar fractions $c_{i\,eq}^*$ (matrix and precipitates) as well as volume fractions (g_ϕ^{eq}) were determined by assuming that the system was in equilibrium just before their respective onset peak temperatures in DSC runs. The value of $\bar{c}_i$ was estimated by assuming that the "new" phase was inactive when computing the equilibrium. The onset temperatures of the peaks associated with the GP zones + β″ + Q′, θ′ and θ phases were found to be respectively equal to 180 °C, 200 °C, and 315 °C. The equilibrium values at these temperatures were calculated with MatCalc using the database assessed by Povoden-Karadeniz [38]. The numerical values obtained are given in the Appendix A section. The molar volume (V_m) of precipitates was assumed constant and equal to 1×10^{-5} m^3/mol. The number density *N0* was estimated from TEM observations obtained on samples aged at 190 °C (Table 4) expect for GP zones. The number density of GP zones was estimated from Biswas et al. [39], who found a value of $1.77 \pm 0.1 \times 10^{22}$ m^{-3} on their binary Al-4 wt%Cu (low iron). This number was multiplied by 4, according to the fact that there was four times more θ′-Al_2Cu in the multicomponent

AlSi7Cu3.5Mg0.15 (Mn, Zr, V) alloy than in the binary Al-3.5 wt%Cu alloy aged at 190 °C. Notice that Biswas et al. [39] determined a number density of θ′-Al_2Cu aged 8 h at 190 °C that was approximately 10 times larger than the one obtained by Heugue et al. [22] in the Al-3.5 wt%Cu alloy aged 12 h at 190 °C.

In this study, we assumed that the GP zones include the θ′′ phase [40,41] and had the stoichiometric composition Al_3Cu. The mean chemical composition of the Q′ phase used in the present study was Al:Mg:Si:Cu = 4:6:6:1 [6,10]. Finally, the appropriate kinetic parameters E and k_0 were taken from the results given in Table 3. Figure 9a presents the evolution of the interfacial mobility with temperature for the different age hardening precipitates. For the sake of comparison, the interfacial mobility curves obtained for the Al-3.5 wt%Cu are presented in Figure 9b. The vertical bars represent the error margin introduced by a ±3 °C uncertainty in the determination of peak temperatures used for the evaluation of E and k_0 according to the Kissinger analysis. In Kissinger diagrams, maximum and minimum slopes for E and the associated k_0 value have been determined with this ±3 °C peak temperature uncertainty. This methodology provides uncertainties for interfacial mobility evaluation for minimum and maximum values of E and k_0. Notice that the interfacial mobility of phases Q′ and β′′ plotted in Figure 9a were established by considering that the number density of each phase was equal to the combined measured number density, as if the precipitates were 100% Q′ or 100% β′′. Assuming that the combined number density was separated equally between the two populations would have for effect to increase both interfacial mobilities by 26%. The curves plotted for these two phases in Figure 9a give therefore a minimum estimate of their interfacial mobility.

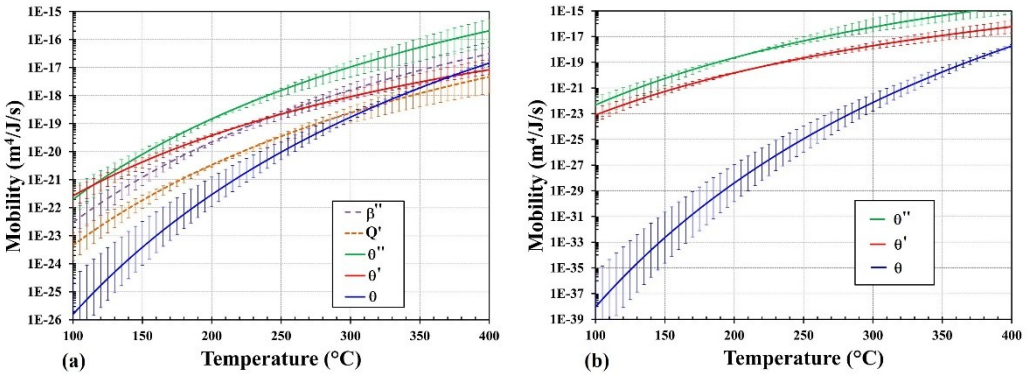

Figure 9. Diagram showing temperature dependency of the interfacial mobility of precipitates (**a**) in the studied AlSi7Cu3.5Mg0.15 (Mn, Zr, V) alloys, (**b**) in the binary Al-3.5 wt%Cu from the previous study (data from [22]).

4. Discussion

4.1. Age Hardening Characterization of AlSi7Cu3.5Mg0.15 (Mn, Zr, V)

Microhardness evolution results during aging, which are depicted in Figure 6a, provide a good demonstration of precipitate hardening. It clearly appears that the maximum hardness is associated with the precipitation of metastable β′′ and Q′ phases (peak A) in the AlSi7Cu3.5Mg0.15 (Mn, Zr, V) alloy. This peak hardening occurs rapidly at 190 °C (<1 h) whereas at such temperature, in binary Al–Cu alloys, peak hardening occurs only after some hours [42] and is mainly associated with the precipitation of θ′ phases.

4.2. Calorimetric Precipitation Study

The kinetic parameters determined by the Kissinger analysis are very important as they help to provide a prediction of the fraction transformed as a function of time during an isothermal aging. Different values of the activation energies were reported in the literature for θ′-Al_2Cu [43–45] and

θ-Al_2Cu [43] for binary Al–Cu alloys. In the binary Al-3.5 wt%Cu alloy studied in our previous study [22], the fraction transformed of GP zones and θ′-Al_2Cu started to rise significantly after respectively 0.2 h and 3 h at 190 °C. At 350 °C, GP zones and θ′-Al_2Cu formed almost instantaneously but the fraction transformed of θ-Al_2Cu rose significantly after 10 h. Another important difference between the DSC curves obtained on alloys Al-3.5 wt%Cu and AlSi7Cu3.5Mg0.15 (Mn, Zr, V) alloy is the intensity of peak A, which is more important in the latter. This is explained by the concomitant and combined precipitation of GP zones, β′′, and Q′ in peak A for the AlSi7Cu3.5Mg0.15 (Mn, Zr, V) alloy. Indeed, it was considered that peak A is caused by the growth of GP zones + β′′ + Q′ while peak B is caused by the growth of θ′-Al_2Cu precipitate. The activation energies associated with the precipitation kinetics of peak A is 100 kJ/mol and the value obtained for θ′-Al_2Cu (peak B) is 76 kJ/mol for the AlSi7Cu3.5Mg0.15 (Mn, Zr, V) alloy. These two values are smaller compared to those determined on the binary Al-3.5 wt%Cu alloy (Table 5). The activation energy determined for the θ-Al_2Cu phase (peak C) was found to be 148 kJ/mol in the multicomponent alloy, which is less than half the value obtained for θ-Al_2Cu in the binary Al-3.5 wt%Cu alloy (330 kJ/mol) (Table 5). But it appears that the activation energy associated to the peak C of the AlSi7Cu3.5Mg0.15 (Mn, Zr, V) alloy is in agreement with one study made on a similar alloy [43]. When compared to the binary Al-3.5 wt%Cu alloy, the faster kinetics of peaks A and B observed on the AlSi7Cu3.5Mg0.15 (Mn, Zr, V) alloy translates into a faster increase of transformed fraction during isothermal aging, which is confirmed by the rapid increase of microhardness evolutions obtained during aging at 190 °C (see Figure 6a). Such a rapid increase of microhardness was also reported by [13,34–36] for Al–Si–Cu alloys. This indicates that the presence of Si is likely the root cause of the acceleration of precipitation hardening in these alloys. The acceleration of the precipitation kinetics in the multicomponent alloy is also very clear for peak C, which results from the growth of the θ-Al_2Cu precipitates. The predicted transformed fraction of θ-Al_2Cu during aging at 350 °C (Figure 6b) rise in a significant manner right at the beginning of aging, while for the Al-3.5 wt%Cu alloy, it took at least 10 h to obtain a significant rise of the fraction transformed at the same temperature. It appears therefore that, due to differences in Si content [46,47], the growth of θ-Al_2Cu precipitates occurs extremely faster in AlSi7Cu3.5Mg0.15 (Mn, Zr, V) alloy than in a binary Al–Cu alloy.

Table 5. Parameters from the fitting procedure for the binary Al-3.5 wt%Cu alloy, data from [22].

Peak	Precipitate	E (kJ/mol)	k_0 (s^{-1})	n	c	Δh (mJ)
A	GP zones	127.81	1.029×10^{11}	3	1	1.490
B	θ′	114.25	2.255×10^{8}	3	1.7	31.66
C	θ	329.55	1.518×10^{22}	3	4	3.476

Biswas et al. [39] found via atom-probe tomography and first-principles calculations that Si atoms tend to substitute with Cu lattice sites of θ′-Al_2Cu phase in Al–Cu–Si alloys. The significant change in the growth kinetics of θ′-Al_2Cu precipitates with high amount of Si could then be attributed to the ability of Si atoms to better accommodate the generation of ledges, because of the excess energy involved by the presence of Si atoms at the interface. The acceleration of ledge formation results in an increase of the interfacial mobility.

4.3. Nanoscale Precipitates Observations by TEM

The size and number density of θ′-Al_2Cu precipitates observed in the AlSi7Cu3.5Mg0.15 (Mn, Zr, V) alloy aged 6 h at 190 °C differ from those reported for the Al-3.5 wt%Cu alloy aged at the same temperature and time. Compared to the values reported for the Al-3.5 wt%Cu alloy, the θ′-Al_2Cu precipitates are smaller (105 versus 171 nm) and more numerous (6.8×10^{20} versus 2.0×10^{20} m^{-3}) in the AlSi7Cu3.5Mg0.15 (Mn, Zr, V) alloy than in the binary alloy. This can be explained by the fact that Si atoms induce more crystal defects and help the multiplication of germination/clustering sites. Notice that the multiplication of nucleation sites depends on the energy involved in the formation of

these sites and not by the interfacial mobility and coefficients of diffusion. After an isothermal aging at 350 °C, θ′-Al_2Cu precipitates are almost completely dissolved after 1 h in the AlSi7Cu3.5Mg0.15 (Mn, Zr, V) alloy as this can be seen in Figure 7c. In the binary Al-3.5 wt%Cu however, the θ′-Al_2Cu precipitates are not dissolved at all after an isothermal aging of 1 h at 350 °C, as this is confirmed in Figure 10. Notice that this picture was obtained with the binary alloy studied in our previous report [22]. The acceleration of the precipitation kinetics in the AlSi7Cu3.5Mg0.15 (Mn, Zr, V) alloy has clearly promoted the dissolution of the θ′-Al_2Cu precipitates in favor of the stable θ-Al_2Cu precipitates. Figure 8 shows that remnant Al_3(Zr, V, Ti) dispersoids and Si precipitates are observed after an isothermal aging of 1 h at 350 °C. It was reported that the precipitation kinetics of Silicon particles has a long incubation period. These precipitates can only be visualized after aging at high temperatures as explained in [48]. The Al_3(Zr, V, Ti) phase seems to remain unalterable with time. The formation of these dispersoids likely occurs inside the matrix during the SHT or during solidification at a very high temperature (>500 °C), as exposed in the work of Rahimian et al. [49].

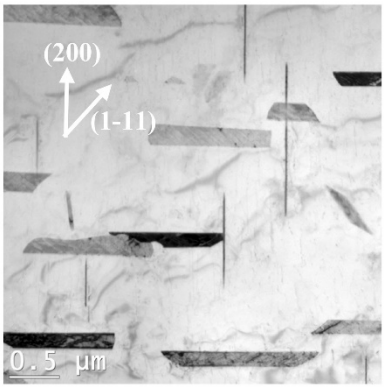

Figure 10. TEM observations on a binary Al-3.5 wt%Cu alloy aged 1 h at 350 °C along the axis <011> in g200 beam condition.

4.4. Interfacial Mobility Calculations

According to Larouche [21], the interfacial mobility impacts the precipitation kinetics essentially at the start of the growth process, which includes the subcritical growth regime [50]. Its impact diminishes significantly once the precipitate reaches a certain size, beyond which the growth process becomes mainly diffusion-controlled. Hence, the interfacial mobility mainly impacts the duration of the incubation period. For isothermal aging, this means that phases with a lower interfacial mobility will have a longer incubation period. The initial growth velocity of the principal semi-axis of a disk-shaped precipitate can be estimated with the following equation [21]:

$$\upsilon_0 = \frac{MRT}{V_m} \sum_{i=1}^{I} c_\theta^i \cdot \ln\left(\frac{\bar{c}_i}{c^*_{i\,eq}}\right). \quad (6)$$

Table 6 presents some values of υ_0 calculated with Equation (6) for θ′ and θ precipitates in the two alloys considered above (binary and multicomponent). The growth velocities of embryos in the multicomponent alloy are systematically larger than in the binary alloy, and by a factor that depends on temperature. Higher values of υ_0 do not mean that the precipitates will have a larger size after a certain time because the size depends on other factors like the number density and the actual shape of the precipitates. The interfacial mobility of the precipitates was estimated by making a major simplification on the evolution of the shape of the precipitates. For the θ′ precipitates for instance, we have assumed that their shape can be modelled as oblate spheroids having an aspect ratio of 20. The contour of such precipitates is a circle, but it is clear that the majority of the real θ′ precipitates does not have a circular contour, as this can be seen in the projection of the precipitates appearing in Figure 10 (the horizontally

aligned precipitates are inclined 45 degrees with respect of the [200] axis). For that obvious reason, the interfacial mobilities plotted in Figure 9 are only rough estimates of the actual ones. Moreover, it is more than likely that interfacial mobility depends on the direction of growth, which implies that the growth is not shape preserved, particularly at the start of the growth process. This said, we think that future developments in the theory of precipitation kinetics will have to consider this parameter to explain the impact of interaction between the interface and dislocations, solute elements, and other defects on the growth rate of precipitates. We consider that trying to model precipitation kinetics by adjusting the interfacial energy to fit the data is leading to an impasse because of the unavoidable discrepancies that will be obtained between different fitted values of this fundamental thermodynamic variable. The interfacial mobility is not a thermodynamic variable. It is just a phenomenological parameter. In the long term, its use will bring more consistency in precipitation kinetics prediction without questioning the values of the interfacial energy.

Table 6. Estimation of the initial growth velocity υ_0 of θ′ and θ precipitates at different temperatures in two alloys containing 3.5 wt%Cu.

Temperature (°C)	Precipitate	Al-3.5wt%Cu	AlSi7Cu3.5Mg0.15 (Mn, Zr, V)
		υ_0 (nm/h)	υ_0 (nm/h)
200	θ′	20	58
235	θ′	148	221
315	θ	0.07	48
400	θ	365	2171

5. Conclusions

The aim of this work was the application of the methodology developed in a previous study to characterize the precipitation kinetics in a more complex aluminum alloy using differential scanning calorimetry (DSC) in order to predict the incubation times during isothermal aging and finally calculate the interfacial mobility of precipitates. Precipitation sequences in both alloys have generally been investigated and the results may be summarized as follows:

- DSC runs of AlSi7Cu3.5Mg0.15 (Mn, Zr, V) alloy present three major exothermic events (peaks A, B, C). These peaks correspond respectively to the growth of GP zones + β′′ + Q′, θ′ and θ.
- The activation energies for θ′-Al_2Cu and θ-Al_2Cu are in the range of 76 and 148 kJ per mol, respectively, for the AlSi7Cu3.5Mg0.15 (Mn, Zr, V), which are significantly less than those reported previously on the binary Al-3.5 wt%Cu alloys [22].
- Si-containing Al_3(Zr, V, Ti) precipitates are present in the AlSi7Cu3.5Mg0.15 (Mn, Zr, V) alloy microstructure for all tested aging conditions.
- Si content in the dendrite has a detrimental impact on the life of metastable precipitates. Indeed, high Si content in a casting alloy helps to get the stable θ-Al_2Cu precipitates faster. It also generates short incubation times for θ′-Al_2Cu.

Author Contributions: Investigation, P.H. and D.L.; Methodology, D.L.; Resources, F.B.; Supervision, D.L., F.B., D.M. and R.M.; Writing—original draft, P.H.; Writing—review & editing, D.L., D.M. and X.G.C.

Funding: This research was funded by the Natural Sciences and Engineering Research Council of Canada (NSERC), grant number RDCPJ 468550—548 14, and also by the companies Montupet and Rio Tinto Arvida.

Acknowledgments: The authors would like to thank Jean-Philippe Masse from $(CM)^2$ at École Polytechnique of Montreal for his strong collaboration in conducting the TEM observations and also Daniel Marcotte, Nathalie Moisan, Hervé Plancke and Marc Choquette for sharing their valuable knowledge and technical expertise.

Conflicts of Interest: The authors declare no conflict of interest.

Appendix A

Molar fractions of elements and volume fraction of phases calculated by MatCalc and the database mc_al.tdb [38].

Table A1. For the AlSi7Cu3.5Mg0.15 (Mn, Zr, V) alloy.

Phases	$c^*_{i\,eq}$ of Matrix				g^{eq}_{Φ}
	Al	Si	Cu	Mg	
At 175 °C					
GP zones	0.975	0.0139	0.00736	$1.63.10^{-3}$	0.0384
β″	0.971	0.0121	0.0147	$2.23.10^{-5}$	0.00495
Q′	0.969	0.0135	0.0149	$4.83.10^{-7}$	0.00398
At 200 °C					
θ′	0.980	0.0154	0.000563	0.0017829	0.0440
At 315 °C					
θ	0.978	0.0153	0.00268	0.0017723	0.0383
	$\bar{c}_i$ of matrix				
SHT 505°C	**Al**	**Si**	**Cu**	**Mg**	
Matrix at 175 and 200 °C	0.966	0.0147	0.0152	0.00170	
Matrix+θ′ at 315 °C	0.980	0.0140	0.00333	0.000109	
	c^i_{Φ} of precipitate ϕ				
	Al	**Si**	**Cu**	**Mg**	
GP zones	0.75		0.25		
β″	0.03	0.51	-	0.45	
Q′	0.235	0.0588	0.353	0.353	
θ′	0.667	-	0.333	-	
θ	0.667	-	0.333	-	

Table A2. Binary Al-3.5 wt%Cu alloy, data from [22].

Phases	$c^*_{i\,eq}$ of Matrix		g^{eq}_{Φ}
	Al	Cu	
At 175 °C			
GP zones	0.993	0.00693	0.0339
At 235 °C			
θ′	0.999	0.000843	0.0431
At 400 °C			
θ	0.994	0.00576	0.0295
	$\bar{c}_i$ of matrix		
SHT 550 °C	**Al**	**Cu**	
Matrix at 175 and 235 °C	0.985	0.0152	
Matrix+ θ′ at 400 °C	0.992	0.00779	
	c^i_{Φ} of precipitate ϕ		
	Al	**Cu**	
GP zones	0.75	0.25	
θ′	0.667	0.333	
θ	0.667	0.333	

References

1. Javidani, M. Effect of Cu, Mg and Fe on Solidification Processing and Microstructure Evolution of Al-7Si Based Foundry Alloys. Ph.D. Thesis, Université Laval, Québec, QC, Canada, 2015.
2. Mohamed, A.M.A.; Samuel, F.H. A review on the heat treatment of Al-Si-Cu-Mg casting alloys. In *Heat Treatment—Conventional and Novel Applications*; Czerwinski, F., Ed.; InTech: Rijeka, Croatia, 2012.
3. Manente, A.; Timelli, G. Optimizing the heat treatment process of cast aluminium alloys. In *Recent Trends in Processing and Degradation of Aluminium Alloys*; Ahmad, Z., Ed.; InTech: Rijeka, Croatia, 2011; pp. 197–220.
4. Porter, D.A.; Easterling, K.E.; Sherif, M.Y. *Phase Transformations in Metals and Alloys*, 3rd ed.; CRC Press: Boca Raton, FL, USA, 2009; p. 520.
5. Dutta, I.; Allen, S.M.; Hafley, J.L. Effect of reinforcement on the aging response of cast 6061 Al-Al2O3 particulate composites. *Metall. Mater. Trans. A* **1991**, *22*, 2553–2563. [CrossRef]
6. Eskin, D.G. Decomposition of supersaturated solid solutions in Al–Cu–Mg–Si alloys. *J. Mater. Sci.* **2003**, *38*, 279–290. [CrossRef]
7. Ding, L.; Jia, Z.; Zhang, Z.; Sanders, R.E.; Liu, Q.; Yang, G. The natural aging and precipitation hardening behaviour of Al-Mg-Si-Cu alloys with different Mg/Si ratios and Cu additions. *Mater. Sci. Eng. A* **2015**, *627*, 119–126. [CrossRef]
8. Xiao, Q.; Liu, H.; Yi, D.; Yin, D.; Chen, Y.; Zhang, Y.; Wang, B. Effect of Cu content on precipitation and age-hardening behavior in Al-Mg-Si-xCu alloys. *J. Alloys Compd.* **2017**, *695*, 1005–1013. [CrossRef]
9. Chakrabarti, D.J.; Laughlin, D.E. Phase relations and precipitation in Al–Mg–Si alloys with Cu additions. *Prog. Mater Sci.* **2004**, *49*, 389–410. [CrossRef]
10. Matsuda, K.; Uetani, Y.; Sato, T.; Ikeno, S. Metastable phases in an Al-Mg-Si alloy containing copper. *Metall. Mater. Trans. A* **2001**, *32A*, 1293–1299.
11. Ding, L.; Jia, Z.; Nie, J.-F.; Weng, Y.; Cao, L.; Chen, H.; Wu, X.; Liu, Q. The structural and compositional evolution of precipitates in Al-Mg-Si-Cu alloy. *Acta Mater.* **2018**, *145*, 437–450. [CrossRef]
12. Sepehrband, P.; Mahmudi, R.; Khomamizadeh, F. Effect of Zr addition on the aging behavior of A319 aluminum cast alloy. *Scr. Mater.* **2005**, *52*, 253–257. [CrossRef]
13. Mahmudi, R.; Sepehrband, P.; Ghasemi, H.M. Improved properties of A319 aluminum casting alloy modified with Zr. *Mater. Lett.* **2006**, *60*, 2606–2610. [CrossRef]
14. Shaha, S.K.; Czerwinski, F.; Kasprzak, W.; Friedman, J.; Chen, D.L. Microstructure and mechanical properties of Al–Si cast alloy with additions of Zr–V–Ti. *Mater. Des.* **2015**, *83*, 801–812. [CrossRef]
15. Elhadari, H.A.; Patel, H.A.; Chen, D.L.; Kasprzak, W. Tensile and fatigue properties of a cast aluminum alloy with Ti, Zr and V additions. *Mater. Sci. Eng. A* **2011**, *528*, 8128–8138. [CrossRef]
16. Litynska, L.; Abou-Ras, D.; Kostorz, G.; Dutkiewicz, J. TEM and HREM study of Al3Zr precipitates in an Al-Mg-Si-Zr alloy. *J. Microsc.* **2006**, *223*, 182–184. [CrossRef] [PubMed]
17. Kozeschnik, E. *Modeling Solid-State Precipitation*; Momentum Press: New York, NY, USA, 2013.
18. Aaronson, H.I.; Enomoto, M.; Lee, J.K. *Mechanisms of Diffusional Phase Transformations in Metals and Alloys*; Taylor & Francis: Boca Raton, FL, USA, 2010; p. 667.
19. Vaithyanathan, V.; Wolverton, C.; Chen, L.Q. Multiscale modeling of θ′ precipitation in Al–Cu binary alloys. *Acta Mater.* **2004**, *52*, 2973–2987. [CrossRef]
20. Chen, Q.; Wu, K.; Sterner, G.; Mason, P. Modeling precipitation kinetics during heat treatment with calphad-based tools. *J. Mater. Eng. Perform.* **2014**, *23*, 4193–4196. [CrossRef]
21. Larouche, D. Mixed mode growth of an ellipsoidal precipitate: Analytical solution for shape preserving growth in the quasi-stationary regime. *Acta Mater.* **2017**, *123*, 188–196. [CrossRef]
22. Heugue, P.; Larouche, D.; Breton, F.; Martinez, R.; Chen, X.G. Evaluation of the growth kinetics of θ′ and θ-Al2Cu precipitates in a binary Al-3.5 Wt Pct Cu alloy. *Metall. Mater. Trans. A* **2019**, *50*, 3048–3060. [CrossRef]
23. Lombardi, A.; D'Elia, F.; Ravindran, C.; MacKay, R. Replication of engine block cylinder bridge microstructure and mechanical properties with lab scale 319 Al alloy billet castings. *Mater. Charact.* **2014**, *87*, 125–137. [CrossRef]
24. Vander Voort, G.F. *Metallography and Microstructures*; ASM International: Materials Park, OH, USA, 2004; Volume 9.

25. Samuel, E.; Samuel, A.M.; Doty, H.W.; Valtierra, S.; Samuel, F.H. Intermetallic phases in Al–Si based cast alloys: New perspective. *Int. J. Cast Met. Res.* **2014**, *27*, 107–114. [CrossRef]
26. Starink, M.J.; Zahra, A.M. Mechanisms of combined GP zone and theta' precipitation in an Al-Cu alloy. *J. Mater. Sci. Lett.* **1997**, *16*, 1613–1615. [CrossRef]
27. Andersson, J.-O.; Helander, T.; Hoglund, L.; Shi, P.; Sundman, B. Thermo-Calc & DICTRA, computational tools for materials science. *Calphad* **2002**, *26*, 273–312.
28. *TTAL7, TT Al-based Alloys Database, version 7.0*; ThermoTech Ltd., Surrey Technology Center: Guildford, UK, 2010.
29. Lee, E.S.; Kim, Y.G. A transformation kinetic model and its application to Cu-Zn-Al shape memory alloys-I. Isothermal conditions. *Acta Metall. Mater.* **1990**, *38*, 1669–1676. [CrossRef]
30. Starink, M.J.; Zahra, A.M. An analysis method for nucleation and growth controlled reactions at constant heating rate. *Thermochim. Acta* **1997**, *292*, 159–168. [CrossRef]
31. Chen, S.P.; Mussert, K.M.; Van Derzwaag, S. Precipitation kinetics in Al6061 and Al6061-alumina particle composite. *J. Mater. Sci.* **1998**, *33*, 4477–4483. [CrossRef]
32. Kozeschnik, E.; Svoboda, J.; Fratzl, P.; Fischer, F.D. Modelling of kinetics in multi-component multi-phase systems with spherical precipitates: II: Numerical solution and application. *Mater. Sci. Eng. A* **2004**, *385*, 157–165.
33. Wang, S.C.; Starink, M.J. Precipitates and intermetallic phases in precipitation hardening Al–Cu–Mg–(Li) based alloys. *Int. Mater. Rev.* **2005**, *50*, 193–215. [CrossRef]
34. Ibrahim, M.F.; Samuel, E.; Samuel, A.M.; Al-Ahmari, A.M.A.; Samuel, F.H. Metallurgical parameters controlling the microstructure and hardness of Al–Si–Cu–Mg base alloys. *Mater. Des.* **2011**, *32*, 2130–2142. [CrossRef]
35. Tavita-Medrano, F.J. Artificial Treatments of 319-Type Aluminum Alloys. Ph.D. Thesis, McGill University, Montreal, QC, Canada, February 2007.
36. Ovono Ovono, D. Recyclabilité des Alliages D'aluminium de Fonderie: Influence des éLéMents RéSiduels sur la Microstructure et le Comportement Mécanique. Ph.D. Thesis, Université de Technologie de Compiègne, Compiègne, France, 2004.
37. Tabibian, S.; Charkaluk, E.; Constantinescu, A.; Guillemot, G.; Szmytka, F. Influence of process-induced microstructure on hardness of two Al–Si alloys. *Mater. Sci. Eng. A* **2015**, *646*, 190–200. [CrossRef]
38. Povoden-Karadeniz, E. *Thermodynamic Data from MatCalc Database 'mc_al.tdb'*, 2.030 ed.; MatCalc Engineering: Vienna, Austria, 2015.
39. Biswas, A.; Siegel, D.J.; Wolverton, C.; Seidman, D.N. Precipitates in Al–Cu alloys revisited: Atom-probe tomographic experiments and first-principles calculations of compositional evolution and interfacial segregation. *Acta Mater.* **2011**, *59*, 6187–6204. [CrossRef]
40. Bastow, T.J.; Celotto, S. Structure evolution in dilute Al(Cu) alloys observed by 63Cu NMR. *Acta Mater.* **2003**, *51*, 4621–4630. [CrossRef]
41. Sun, D.; Wang, Y.; Zhang, X.; Zhang, M.; Niu, Y. First-principles calculation on the thermodynamic and elastic properties of precipitations in Al-Cu alloys. *Superlattices Microstruct.* **2016**, *100*, 112–119. [CrossRef]
42. Silcock, J.M.; Heal, T.J.; Hardy, H.K. Structural ageing characteristics of aluminum-copper alloys. *J. Inst. Met.* **1954**, *82*, 239–248.
43. Barlas, B. Etude du Comportement et de L'endommagement en Fatigue D'alliages D'aluminium de Fonderie. Ph.D. Thesis, Ecole Nationale Supérieure des Mines de Paris, Evry, France, 5 February 2004.
44. Smith, G.W. Precipitation kinetics in an air-cooled aluminum alloy: A comparison of scanning and isothermal calorimetry measurement methods. *Thermochim. Acta* **1998**, *313*, 27–36. [CrossRef]
45. Ovono Ovono, D.; Guillot, I.; Massinon, D. Determination of the activation energy in a cast aluminium alloy by TEM and DSC. *J. Alloys Compd.* **2007**, *432*, 241–246. [CrossRef]
46. Liu, L.; Chen, J.H.; Wang, S.B.; Liu, C.H.; Yang, S.S.; Wu, C.L. The effect of Si on precipitation in Al–Cu–Mg alloy with a high Cu/Mg ratio. *Mater. Sci. Eng. A* **2014**, *606*, 187–195. [CrossRef]
47. Gupta, A.K.; Lloyd, D.J.; Court, S.A. Precipitation hardening in Al–Mg–Si alloys with and without excess Si. *Mater. Sci. Eng. A* **2001**, *316*, 11–17. [CrossRef]
48. Hernandez Paz, J.F. Heat Treatment and Precipitation in A356 Aluminum Alloy. Ph.D. Thesis, McGill University, Montreal, QC, Canada, September 2003.

49. Rahimian, M.; Amirkhanlou, S.; Blake, P.; Ji, S. Nanoscale Zr-containing precipitates; a solution for significant improvement of high-temperature strength in Al-Si-Cu-Mg alloys. *Mater. Sci. Eng. A* **2018**, *721*, 328–338. [CrossRef]
50. Larouche, D. A new theory of the solid-state growth of embryos during nucleation: The fundamental role of interfacial mobility. *Philos. Mag.* **2018**, *98*, 2035–2060. [CrossRef]